ADVANCING EARTH AND SPACE SCIENCES

JGR Space Physics

RESEARCH ARTICLE
10.1029/2025JA033838

Special Collection:
Solar Wind: Origin, Acceleration, and Outflow

Core-Halo Correlations of Solar Wind Electrons and Temperature Anisotropy Instabilities

S. M. Shaaban[1], S. Kennis[2], M. Lazar[2,3], V. Pierrard[4,5], and S. Poedts[2,6]

[1]Department of Physics and Materials Sciences, College of Arts and Sciences, Qatar University, Doha, Qatar, [2]Centre for Mathematical Plasma Astrophysics, KU Leuven, Leuven, Belgium, [3]Institut für Theoretische Physik IV, Ruhr-Universität Bochum, Bochum, Germany, [4]Royal Belgian Institute for Space Aeronomy (BIRA-IASB), Space Physics, Solar-Terrestrial Center of Excellence, Brussels, Belgium, [5]Earth and Life Institute—Climate Sciences (ELI-C), Université Catholique de Louvain, Louvain-la-Neuve, Belgium, [6]Institute of Physics, University of Maria Curie-Skłodowska, Lublin, Poland

Key Points:

- Observed electron core and halo populations in the solar wind are correlated by kinetic parameters, temperature anisotropy and plasma beta
- Thresholds of temperature anisotropy instabilities can be significantly reduced under the mutual core-halo effects
- Comparisons with observations prove the constraining role of self-generated instabilities for the low-energy core and the suprathermal halo

Correspondence to:
S. M. Shaaban,
shamd@qu.edu.qa;
s.m.shaaban88@gmail.com

Citation:
Shaaban, S. M., Kennis, S., Lazar, M., Pierrard, V., & Poedts, S. (2025). Core-halo correlations of solar wind electrons and temperature anisotropy instabilities. *Journal of Geophysical Research: Space Physics*, *130*, e2025JA033838. https://doi.org/10.1029/2025JA033838

Received 11 FEB 2025
Accepted 23 APR 2025

Abstract The properties of electrons in the heliospheric plasma are modulated by various factors, starting with the expansion and bimodal nature of the slow or fast solar wind, and continuing with the kinetic mechanisms of acceleration and energy exchange with small-scale plasma waves. The role of wave-particle interactions can be understood through rigorous kinetic modeling based on observational data. This paper presents a refined evaluation of the instabilities triggered by temperature anisotropy, that is, whistler and firehose instabilities, taking into account for the first time the correlations between the electron core and halo populations revealed by in situ observations. In establishing core-halo correlations, temperature anisotropies (A) and plasma beta parameters $\left(\beta_{\parallel}\right)$ are of interest, as quantifiers of free (kinetic) energy at the origin of instabilities. These correlations incorporate the mutual effects of the electron populations and enable a realistic characterization of instabilities, in terms of either the core or the halo parameters. The instability thresholds can be significantly reduced under the mutual core-halo effects, and comparisons with observations prove the constraining role of self-generated instabilities, not only for the core but also for the halo electrons. The most relevant are the results for the slow solar wind, for which both the parameters and the core-halo correlations are less affected by the strahl component, which is otherwise more prominent in the fast wind. In high-speed winds, temperature anisotropies are more confined, most likely under a stronger effect of fluctuations generated by the electron strahl whose properties are not yet quantified to allow a similar analysis.

Plain Language Summary In space plasmas, electrons rarely collide, yet observations show their temperature anisotropies remain largely confined. Recent theories explain this for low-energy core electrons, but face challenges with the hotter, less dense halo population. Our study refines the approach by revealing high correlations between core and halo electron properties, derived from a large data set that spans diverse solar wind conditions. These correlations reshape the thresholds of the instabilities that regulate electron temperature anisotropies. Our results closely match observations of the solar wind, providing the most compelling evidence to date for self-generated instabilities as key constraints on electron dynamics.

1. Introduction

The solar wind is a hot and dilute outflow of charged particles, mainly electrons and protons, expected to be largely (self)controlled by interactions with small-scale plasma waves and fluctuations (Bale et al., 2009; Berčič et al., 2019; Huang et al., 2020; Lazar et al., 2022; Shaaban et al., 2021; Verscharen et al., 2022; Štverák et al., 2008). Because electrons are much lighter than protons, one can easily discriminate between electron populations at different energies and pitch angles in their fluxes (Maksimovic et al., 2005; Pierrard et al., 2000; Wilson et al., 2019a, 2019b; Štverák et al., 2008). Two distinct populations are ubiquitous in observed velocity distributions (VDs), the low-energy core (index c) with high relative density (on average $n_c/n_e > 90\%$) well described by (bi-)Maxwellian distributions (specific to quasi-thermal equilibrium) and a suprathermal population that enhances the high-energy tails of observed VDs and is better reproduced by power-law Kappa distributions (Pierrard & Lazar, 2010). Moreover, in the suprathermal tails, one can identify a halo (index h) more attached to the core, and a strahl (or beam component) aligned to the background magnetic field $(\mathbf{B}_0)$, less symmetric, and generally less dense than the halo. In high-speed solar winds the strahl becomes more prominent and may exceed the halo density. Suprathermal electrons are particularly important, as these populations transport the major heat flux in the solar wind. Despite its low number density (on average $n_h/n_e \sim 5\%$), the halo typically has a high kinetic temperature (or energy), often much higher than the core, that is, $T_h/T_c \gg 1$ (Lazar et al., 2020; Wilson et al., 2019a, 2019b). It can thus be argued that not only the core but also the halo can be equally involved in the kinetic processes, including the wave instabilities triggered by the kinetic anisotropies.

Kinetic instabilities triggered by electron anisotropies have been extensively studied in various contexts in space plasmas, more recently also taking into account the presence of suprathermal populations (Gary, 1993; Lazar et al., 2022; Shaaban et al., 2021; Verscharen, Klein, & Maruca, 2019; Viñas et al., 2015). In the absence of collisions, self-generated instabilities should be the most plausible constraints for the kinetic anisotropies, including electron beams (carrying the heat flux) and temperature anisotropies. The free kinetic energy of the particles is converted into electromagnetic fields, while the resulting growing fluctuations act back, tending to reduce the anisotropy. Collisions are *replaced* by wave-particle interactions, but with different consequences: Wave–particle interactions can accelerate or decelerate charged particles and also (pitch-angle) scatter them, reducing initial anisotropy; but these interactions will never completely isotropize the VDs (Lazar et al., 2022; Shaaban et al., 2021). The kinetic waves and turbulence present in space plasmas cause the distributions to never relax but remain out of thermal equilibrium, generally below the anisotropy thresholds of the kinetic instabilities (Berčič et al., 2019; Shaaban et al., 2019c; Štverák et al., 2008).

For an adequate description of these instabilities, we need to understand the observations, starting with the distinct electron populations. The in situ data suggest physical interconnections via their properties, for example, densities, temperatures, temperature anisotropies, etc. (Abraham et al., 2022; Berčič et al., 2019; Lazar et al., 2020; Maksimovic et al., 2005; Pierrard et al., 2016, 2020, 2022; Štverák et al., 2008, 2009). These interlinks provide clues about the potential role of each population in the kinetic processes of interest, and also about their origin and formation, in particular, the origin of the suprathermal halo, which is still a paradigm (Maksimovic et al., 2021). Thus, at sufficiently large heliocentric distances, for example, >0.3 AU, the relative densities of the halo and strahl populations appear anti-correlated, suggesting an enhancement of the electron halo at the expense of the strahl (Berčič et al., 2019; Maksimovic et al., 2005; Štverák et al., 2009), most probably due to the self-generated instabilities, which scatter and tend to isotropize the beaming (strahl) electrons (Micera et al., 2020; Verscharen, Chandran, et al., 2019). The more recent observations from the young solar wind (<0.5 AU) reveal a similar anti-correlation between the core and halo populations (Abraham et al., 2022), with the halo density increasing more likely as a result of the energization of core electrons through wave-particle interactions (Vocks et al., 2008; Yoon et al., 2016). This may explain why the halo remains more attached to the core even at larger heliocentric distances. Despite this fact, observational analyzes show that their temperatures, and especially their temperature anisotropies, can be very different (Pierrard et al., 2016; Štverák et al., 2008). These are key parameters that quantify the free kinetic energy of electrons as sources of instabilities.

An eloquent example is the spread of the observed electron states in the parametric space of temperature anisotropy $A = T_\perp/T_\|$ versus parallel plasma beta $\beta_\| = 8\pi n_e k_B T_\|/B_0^2$ (where k_B is the Boltzmann constant and $\|, \perp$ indicate components to gyrotropic directions with respect to $\mathbf{B}_0$). These states appear quasi-stable and bounded by the self-generated wave instabilities: The thresholds of the electromagnetic electron-cyclotron (EMEC or whistler) instability constrain the upper anisotropies $A > 1$, while the lower anisotropies $A < 1$ are shaped by the firehose instability (Štverák et al., 2008). The linear theory of wave dispersion and stability applies well enough to the bi-Maxwellian core, as it dominates and remains less affected by the other populations (Shaaban et al., 2019c). However, this is not the case for the suprathermal halo, whose properties are well described by Kappa distributions (Maksimovic et al., 2005; Wilson et al., 2019b; Štverák et al., 2008), but whose implications in kinetic instabilities are not yet adequately interpreted and modeled. The halo population is still concentrated near the equipartition of kinetic and magnetic energies $\left(\beta_\| \sim 1\right)$, but at slightly lower values than the core $\left(\beta_{h\|} \lesssim \beta_{c\|}\right)$. This is because of the much lower density of the halo, which is not always compensated by their higher temperature. Moreover, the temperature anisotropy of halo electrons exhibits a larger spread in A-vs.-$\beta_\|$ diagrams, and the same bi-Maxwellian thresholds were found to be inconclusive (Štverák et al., 2008).

In this case, the approach must be different, first of all considering electrons with a bi-Kappa distribution (Lazar et al., 2018), specific to the halo, and second taking into account, by some means, the influence of the core. The reason is that the massive core can have temperature anisotropies similar to $\left(A_c \sim A_h\right)$, or even opposite to those of the halo, that is, $A_c \lesseqgtr 1$ and $A_h \gtreqless 1$. Shaaban et al. (2019c) have studied temperature anisotropies assuming correlations between the core and halo parameters, such as, for temperature anisotropies $A_c \simeq A_h$, and for plasma betas $\beta_{c\|} = 2.236\beta_{h\|}$ for small $\kappa = 3$, and $\beta_{c\|} = 3.809\beta_{h\|}$ for large $\kappa = 8$. However, these are only approximate (linear) correlations suggested by observations (Lazar et al., 2018; Pierrard et al., 2016), while attempts to consistently determine them are not yet known. If they exist and are rigorously established, these correlations can indeed capture core–halo mutual influences and also facilitate the analysis of instability conditions, as a function of the core or halo parameters (Shaaban et al., 2019c). The instability thresholds calculated in this way, either as a function of A_c and $\beta_{c\|}$ or as a function of A_h and $\beta_{h\|}$, should enable a relevant comparison with the observations.

In the present work, we show that such correlations do exist and quantify them for further use in characterizing the temperature anisotropy instability. For this purpose, we used a comprehensive data set from three missions, Helios I, Cluster II and Ulysses, that covered a wide range of heliocentric distance in the ecliptic, from 0.3 to about 4.0 AU (Štverák et al., 2008). This data set has been widely exploited, not only in observational analyzes of temperature anisotropies (Pierrard et al., 2016; Štverák et al., 2008), but also of variations in densities, temperatures, and suprathermal features with the heliocentric distance and the speed of the solar wind flow (Lazar et al., 2020; Pierrard et al., 2016, 2020, 2022). Our paper is structured as follows. Section 2 contains the results of the observational analysis that establishes the correlations between the main parameters of the core and halo populations. These are the temperature anisotropy and the plasma beta parameters, which intervene explicitly in the wave dispersion and stability theory. The obtained correlations are then applied, in Section 3, to the analysis of whistler and firehose instabilities. The correlations are particularly important for deriving the thresholds of these two instabilities, which are then compared with the relevant observational data. The main conclusions of our analysis are summarized in the last section, Section 4.

2. Observed Core-Halo Correlations

Štverák et al. (2008) extracted from the observed electron VDs the properties of the two main components: The low-energy bi-Maxwellian core and the bi-Kappa suprathermal halo, with power-law tails quantified by the κ exponent. Their properties may also be affected by the strahl, if present, especially in high-speed winds, which may explain the differences found for these properties in fast and slow winds (Lazar et al., 2020; Pierrard et al., 2020, 2022; Štverák et al., 2008) (The strahl properties were not estimated for these events, but it has been argued that the field-aligned strahl is usually directed anti-sunward (Štverák et al., 2008). Thus, it determines an asymmetric skewness of the observed VD along the magnetic field, which contrasts with the more symmetric core and halo populations. Therefore, to fit the core and halo to the bi-Maxwellian and bi-Kappa models, respectively, only the data measured in the sunward direction (not affected by the strahl) were used, assuming that these two populations have the same properties in the antisunward direction). For instance, both the core and the halo populations exhibit lower temperature anisotropies in fast winds, potentially constrained by strahl-driven (or heat flux) instabilities (Shaaban et al., 2019a). The same differentiation is adopted here, with particular interest for the core-halo interplay in slow wind with bulk speed $V_{sw} \leqslant 450$ km/s, when the strahl is expected to have minimal influence. We now examine the parameters needed in the characterization of temperature anisotropy instabilities from Section 3. Through a quantitative approach, we aim to determine how valid the suggestions of previous analyzes are for linear correlations between the core and halo parameters, namely the temperature anisotropies and the plasma beta parameters (Pierrard et al., 2016; Shaaban et al., 2019c).

2.1. Core and Halo Temperature Anisotropies

As previously stated, the temperature may exhibit anisotropies $A = T_\perp / T_\| \neq 1$, which can provide insight into the underlying mechanisms responsible for the deviation from thermal equilibrium, as well as the subsequent instabilities and the role played in the solar wind. Temperature anisotropy quantifies a surplus of perpendicular or parallel temperature, $A > 1$ or $A < 1$, respectively, while $A = 1$ signifies an isotropic temperature. The anisotropies of the core, A_c, and the halo, A_h, were thus calculated and subsequently compared (Pierrard et al., 2016; Štverák et al., 2008). We start from the findings in Pierrard et al. (2016), which showed the tendency of the scatter plots to accumulate around the isotropy condition $A_h = A_c = 1$, and to align with the (first) diagonal of $A_h = A_c$. The same tendency is also shown in our Figures 1 and 2, also in Figures A1–A3 from Appendix A.

Here the degree of correlation between the core and halo anisotropies is quantified by considering their proximity and alignment to the first diagonal of perfect linearly correlated anisotropies $A_c = A_h$, see Figure 1. We used the Pearson correlation coefficient r, to assess the strength and direction of the linear relationships between A_c and A_h (Hinkle et al., 2003). It can vary from $r = 1$ (perfect positive correlation—first diagonal), through $r = 0$ (no

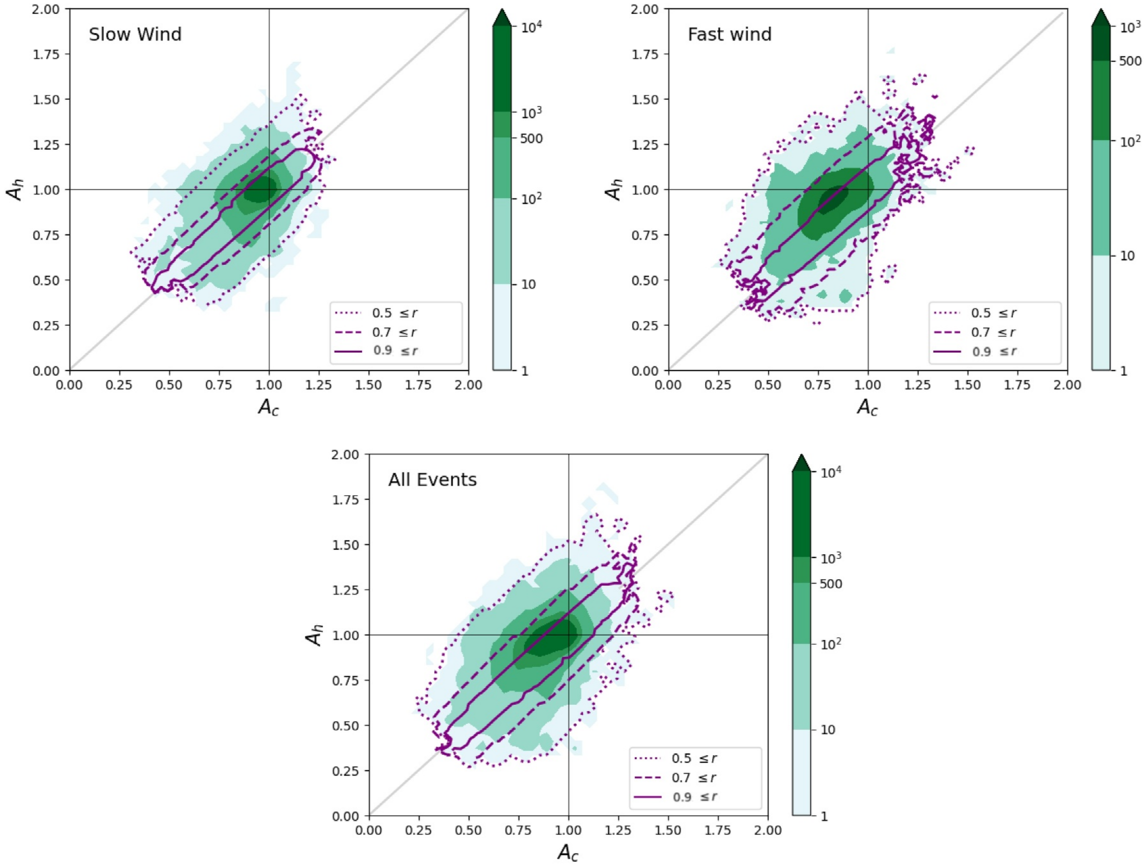

Figure 1. Density plots of the events (greenish color codded) in the slow wind (top-left), fast wind (top-right), and all events (bottom). Contours incorporate three groups of events with correlated anisotropies: moderate with $0.5 \leqslant r < 0.7$ (dotted), high with $0.7 \leqslant r < 0.9$ (dashed), and very high with $r \geqslant 0.9$ (solid).

linear correlation), to $r = -1$ (perfect negative correlation or anticorrelation—second diagonal). In between extreme conditions, the standard interpretation of r applies for the linear correlation: very high for $0.9 \leqslant r \leqslant 1$, high for $0.7 \leqslant r < 0.9$, moderate for $0.5 \leqslant r < 0.7$, low for $0.3 \leqslant r < 0.5$, and negligible for $0.0 \leqslant r < 0.3$ (Hinkle et al., 2003).

In Figure 1 we can recognize the clear tendency shown by all events (bottom panel) to align to the first diagonal (light gray line). The number of events is color-coded, with a darker color meaning more events. Those with very highly correlated anisotropies of the core and halo populations are bordered by the solid (purple) line, and those with high correlations are limited by the dashed line. This trend is visibly more pronounced in the fast solar wind (top-right panel), where all events are inside the dotted contour, showing at least moderate correlation ($r \geqslant 0.5$). Moreover, compared to the slow wind events (top-left panel), the fast wind data tend to accumulate above the first diagonal, where $A_h > A_c$, and also toward the anisotropies in the parallel direction, that is, $A_c < A_h < 1$. In this case, the parallel energy surplus can result from an anomalous adiabatic expansion of the solar wind (Matteini et al., 2007), but also from the relaxation and diffusion of the strahl (Micera et al., 2020). However, it should be mentioned that in this data set, the number of fast wind events (top-right) is lower than the number of slow wind events (top-left). In the slow wind, the events are also distributed along the first diagonal of $A_c = A_h$, but accumulate with a peak number around the isotropy conditions $A_c = A_h = 1$. Also note that the dashed line contour still incorporates a fraction of over 78% highly correlated events, see also Table 1.

In Figure 2 the top panels show the total number of events (right) and selections from slow and fast winds (left and middle panels, respectively). The number of events is color-codded; the lighter the color, the more events are in that location. Particularly interesting are the fractions or the relative number of events with sufficiently highly correlated anisotropies, that is, those in the first two categories mentioned above. These events are also selected in Figure 2, panels at the bottom show those satisfying $r \geqslant 0.9$, while those at the middle row display events with

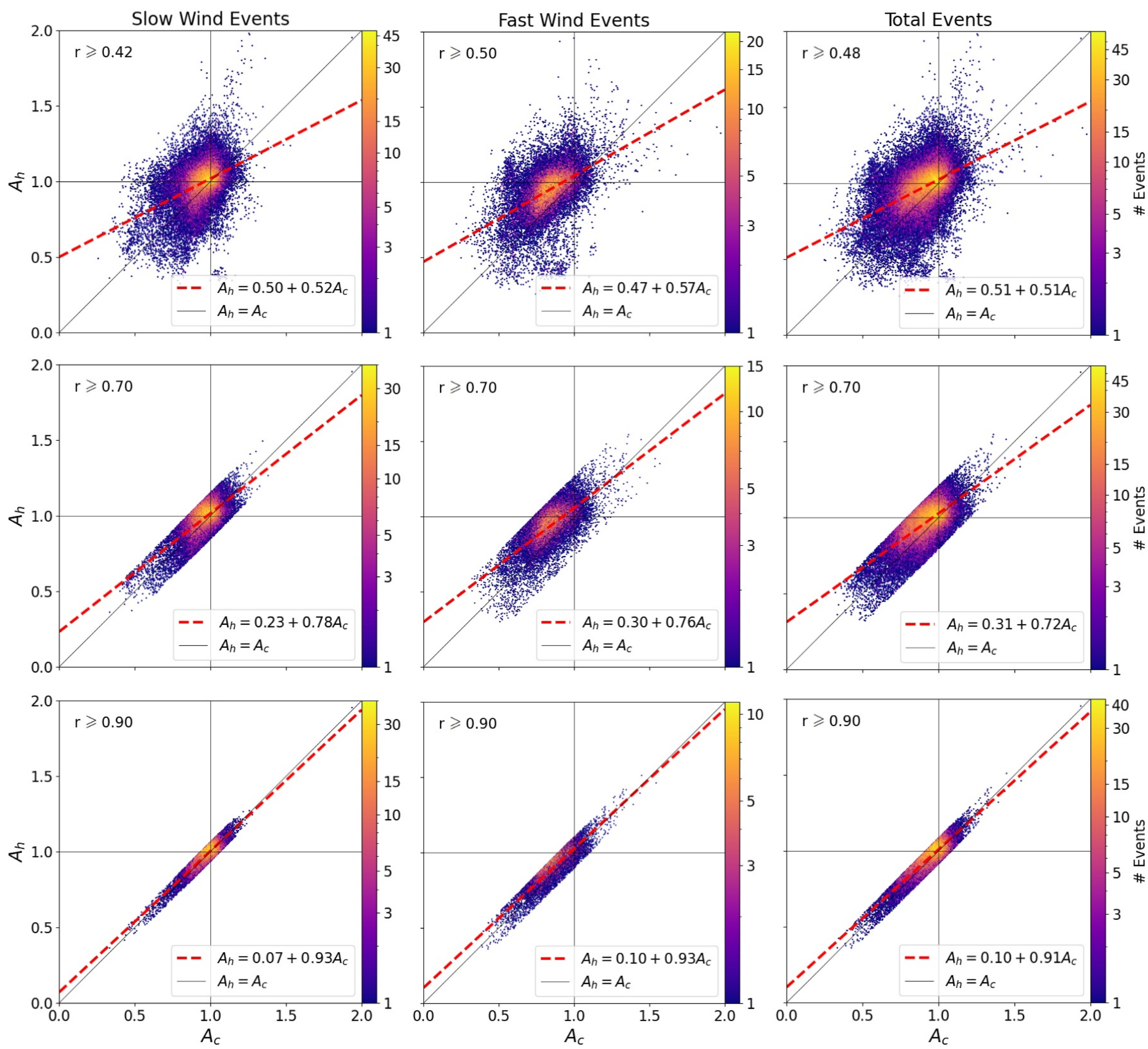

Figure 2. A_h versus A_c for the slow wind (left), fast wind (middle) and total number of events (right). Overlaid are the first diagonal (light gray) indicating $A_h = A_c$, and the linear regression (red dashed) calculated for each data set. Middle row shows only the events with $r \geqslant 0.7$, and lower row those with $r \geqslant 0.9$ (lowest deviation of the linear regression from the first diagonal).

$r \geqslant 0.7$. The corresponding fractional numbers are given in Table 1. The linear regression fit, that is, $A_h = mA_c + q$, is also plotted (red dashed line), with a deviation from the first diagonal that decreases with increasing linear correlation of the selected events. The correlation obtained for the total number of events in the upper panels is naturally lower, and the linear regression is more deviated. Depending on its relevance, linear regression will be used in applications such as characterization of kinetic instabilities. Its relevance is therefore established taking into account a sufficiently high correlation, preferably $r \geqslant 0.7$, but also requires that the high correlation applies to a significant fraction of events. Table 1 thus demonstrates that regardless of the solar wind speed more than 40% of the events are very highly correlated ($r \geqslant 0.9$), and more than 78% of the events are highly correlated ($r \geqslant 0.7$). We note that the linear regression fit does not significantly depend on the nature of the solar wind, fast or slow, also in agreement with the estimates of the fractions of correlated events from Table 1.

In Appendix A, Figures A1–A3 make a further distinction between the events associated with different values of the parameter κ. Thus, in Figures A1 and A2 we select events in intervals around two low values $\kappa = 3$ and 5, such as $\kappa \in [2.7, 3.3]$, and $\kappa \in [4.5, 5.5]$, respectively, while Figure A3 displays the events with $\kappa \geqslant 6$. For each of these three categories, we calculate the fraction of events (in %) with different linear correlations, and the values can be found in Table 2. These fractions are even higher than those (marked) in Table 1, again demonstrating the high degree of linear correlation of the anisotropies. The differentiation in Figures A1–A3 also has relevance for

Table 1
Fraction of Events [%] in the Slow Wind, Fast Wind, and All Data, With Specific Relevance Given by the Range of κ and Linear Correlation r

		Correlated events [%]		
κ	r	Slow wind	Fast wind	All data
[2.7, 3.3]	⩾0.9	1.91	1.77	1.97
[4.5, 5.5]	⩾0.9	5.50	7.25	6.19
[6.3, 7.7]	⩾0.9	13.04	14.63	15.07
[2.7, 7.7]	⩾0.9	20.45	23.65	23.23
all κ	⩾0.9	43.75	40.50	43.62
[2.7, 3.3]	⩾0.7	3.58	2.77	3.40
[4.5, 5.5]	⩾0.7	9.54	15.90	11.70
[6.3, 7.7]	⩾0.7	24.10	32.00	28.21
[2.7, 7.7]	⩾0.7	37.22	50.68	43.31
all κ	⩾0.7	78.22	89.46	85.00
[2.7, 3.3]	⩾0.5	3.98	2.80	3.53
[4.5, 5.5]	⩾0.5	11.10	18.55	13.88
[6.3, 7.7]	⩾0.5	32.38	36.49	35.76
[2.7, 7.7]	⩾0.5	47.46	57.84	53.17
all κ	⩾0.5	97.75	99.94	99.54

Note. The gray shading in Table 1 highlights the data used in Figure 1 and enables direct comparison with similar values in Table 2.

various heliocentric distances, because κ shows a monotonic decrease from 0.3 to 4 AU in the ecliptic (Lazar et al., 2020; Pierrard et al., 2016). This time it can be observed that the linear regression fit line (red dashed) can depend on the nature of the halo populations, indicating an apparent decrease in the correlation of anisotropies with increasing κ. That is, with the thermalization of the electron halo at low heliocentric distances, toward 0.3 AU. This is also confirmed by the corresponding fractions of correlated events in Tables 1 and 2.

2.2. Plasma Beta Parameters

Next we analyze the plasma beta parameters of the core and halo electron populations. The plasma beta parameter represents the ratio between the kinetic energy density of the particle population of sort j, and the magnetic energy density

$$\beta_j = \frac{8\pi n_j k_B T_j}{B_0^2}. \tag{1}$$

k_B is the Boltzmann constant, n_j is the number density, T_j is already known as temperature, and B_0 is the magnitude of the local magnetic field. The plasma beta parameter can be calculated separately, for the core and the halo, and then compared with each other. The core is more dense, but at the same time can be much cooler than the halo, resulting in comparable plasma beta parameters (Lazar & Fichtner, 2021).

The beta parameter can also be calculated for the (gyrotropic) components of the temperature, whose anisotropy we analyzed above. For the study of instabilities and their effects in space plasmas, the parallel component of the beta parameter $\beta_{j\parallel} = 8\pi n_j k_B T_{j\parallel}/B_0^2$ is already used (Shaaban et al., 2019c; Štverák et al., 2008). Therefore, in Figure 3 we represent the values obtained for $\beta_{c\parallel}$ as a function of $\beta_{h\parallel}$, while the number of events is color coded. We again distinguish between events in the slow wind (left), fast wind (center), and all events (right). From top to bottom, the events are counted as a function of the parameter κ, choosing three categories from distinct ranges such as $\kappa \in [2.7, 3.3]$ (top panels), $\kappa \in [4.5, 5.5]$ (second row from top), and $\kappa \geqslant 6$ (third row from top). The bottom panels show the events for all κ values.

To identify the dependencies between the beta parameters of the core and the halo populations, we first note the predominance of the core, generally with $\beta_{c\parallel} > \beta_{h\parallel}$, data lying above the black-solid line (first diagonal) of $\beta_{c\parallel} = \beta_{h\parallel}$. Their large values remain above but tend to align with this diagonal, suggesting that suprathermal particles should have a non-negligible influence on kinetic effects, such as temperature anisotropy instabilities (Lazar & Fichtner, 2021). A higher value of the beta parameter for the core may also suggest that it plays a more significant (kinetic) role in the plasma system than the halo. Second, we take into account the bimodal nature of all the scatter plots in Figure 3: at small values ($\beta_{c\parallel} < 1$ and $\beta_{h\parallel} < 1$) the data seem to align according to a power law, while at values above unity the data show more of a linear dependence of these parameters, more or less parallel to the diagonal $\left(\beta_{c\parallel} = \beta_{h\parallel}\right)$. Thus, the average values of the events (black dots) are used to obtain the power-law fit $\beta_{c\parallel} = a\beta_{h\parallel}^b$ (green line) for $\beta_{h\parallel} \leqslant 0.1$, and the linear fit $\beta_{c\parallel} = c + d\beta_{h\parallel}$ (red line) for $\beta_{h\parallel} > 0.1$. The power-law branch is consistently present in both types of slow or fast solar wind event, while the linear branch is only poorly represented in the fast wind. The values obtained for the fitting parameters a, b, c, d are given in the legends. These values depend on the nature of the solar wind, slow or fast, and also on the range of

Table 2
Fraction of Events [%] With Different Correlation in Each Category Defined by κ Values

		Correlated events [%]		
Events	r	$\kappa \in [2.7, 3.3]$	$\kappa \in [4.5, 5.5]$	$\kappa \geqslant 6$
Total	⩾0.9	57.61	44.77	42.92
	⩾0.7	96.29	89.99	99.27
	⩾0.5	100	99.15	97.96
Slow wind	⩾0.9	48.38	49.76	38.16
	⩾0.7	89.99	86.79	68.32
	⩾0.5	100	99.98	89.37
Fast wind	⩾0.9	64.21	40.14	39.90
	⩾0.7	99.27	86.34	87.93
	⩾0.5	100	99.18	99.97

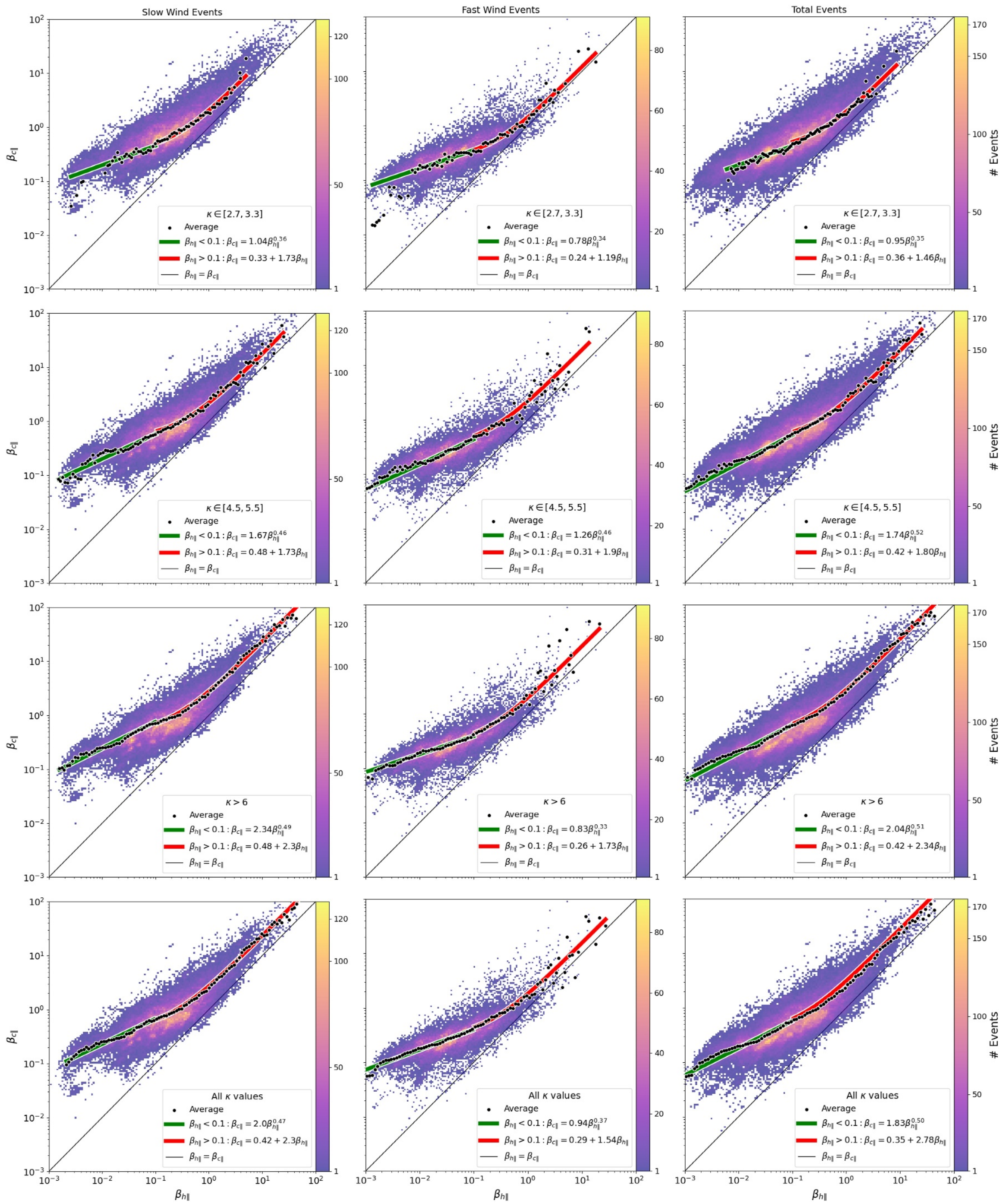

Figure 3. $\beta_{c\|}$ versus $\beta_{h\|}$ for various classes of events (counted by color bars): slow solar winds (v< 450 km/s, left), fast winds (v>450 km/s, center), and the total data (right). These events approach the diagonal of $\beta_{\|c} = \beta_{\|h}$ (solid line), but are in general above it. Events with different κ values are distinguished from top to bottom: $\kappa \in [2.7, 3.3]$ (top), $\kappa \in [4.5, 5.5]$ (second row), $\kappa > 6$ (third row) and all κ values (bottom). Black dots, and the green and red fits are explained in the legends and text.

values of the κ parameter. Regarding the linear branch at high values of the beta parameters, the higher the κ value, the further away the fit is from the diagonal. This suggests that for higher values of κ, which corresponds to a higher proximity to the Sun and a higher thermalization of the halo electrons, the core assumes a more significant role and may dominate in contributing to the kinetic processes. Moreover, $\beta_{c\|}$ remains systematically larger than $\beta_{h\|}$ across all ranges of κ values and different solar wind speeds.

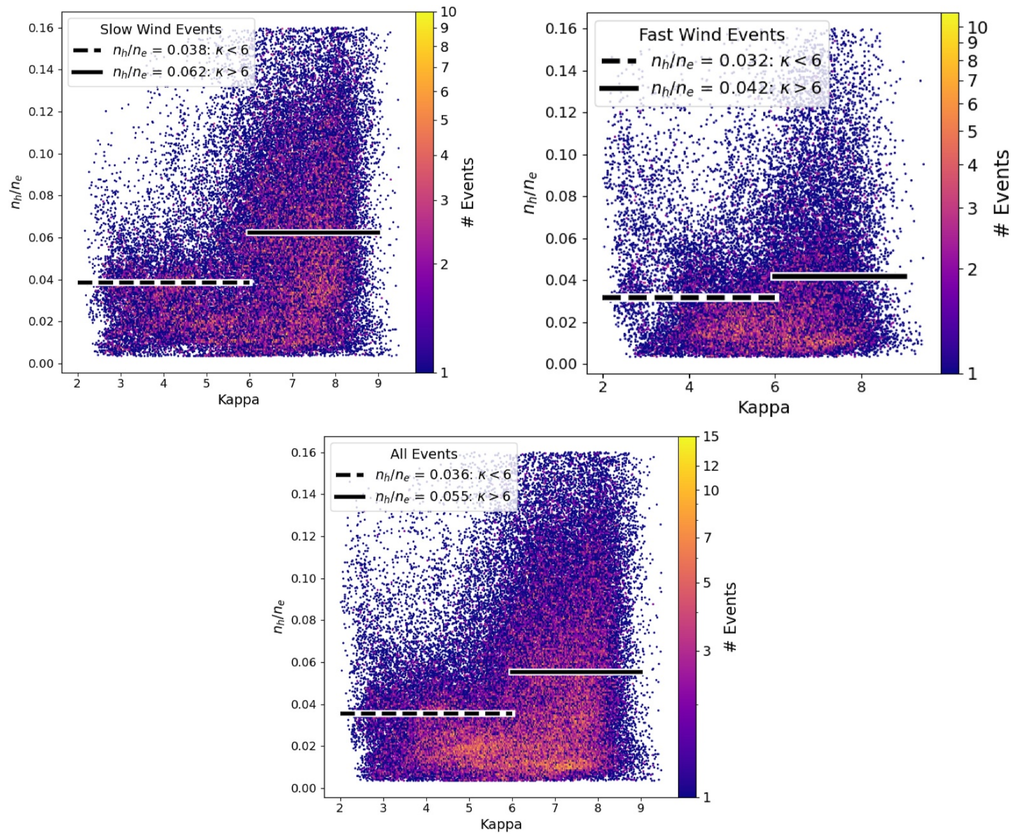

Figure 4. Density plots of η_h as a function of κ for slow wind (top-left), fast wind (top-right) and all events (bottom). Mean values of η_h are obtained for $\kappa < 6$ and $\kappa > 6$, and are indicated with, respectively, dashed and solid lines (also in the legends).

2.3. Relative Halo Density

The last parameter needed to characterize temperature anisotropy instabilities is the relative density, either of the core $\eta_c = n_c/n_e$ or of the halo $\eta_h = n_h/n_e$ (Lazar et al., 2022; Viñas et al., 2015). It is sufficient to determine only one of them, for example, η_h, while the relationship between these two parameters is established by the neutrality of charge, $\eta_c = 1 - \eta_h$. Instead, from the previous results we can learn about the mean values of the relative density $\eta_h = n_h/n_e$, which, in the ecliptic, do not differ much from those of n_h/n_c (Lazar et al., 2020; Pierrard et al., 2020). Thus, in both slow and fast solar winds, these average values show a twofold profile in the variation with the heliocentric distance and implicitly with the parameter κ (specific to the suprathermal halo). For instance, in slow solar winds, the average values of η_h obtained for a predominantly large κ at low distances do not differ much from each other but are higher than those obtained for a small κ at large distances.

Figure 4 shows the relative density of the halo component, η_h, as a function of the parameter κ, for slow winds (top-left panel), fast winds (top-right panel) and all events (bottom panel). The adjacent color bar and numbering indicate the number of events. In the slow solar wind, the events prominently show the same dual clustering: at a more restrained range of low values of η_h, whose mean value $\left(\eta_h = 0.038\right)$ is indicated by the dashed line; and at a much wider range of values, whose mean value $\left(\eta_h = 0.062\right)$ is higher and is indicated with a solid line. The separation between the two data groups is found around $\kappa \simeq 6$. This dual clustering tendency is still prominent in the bottom panel with all events, under the dominance of slow wind data. However, the same tendency is less significant in the fast solar wind (middle panel), which causes the difference between the mean values of the relative density η_h to decrease.

3. Temperature Anisotropy Instabilities

We now focus on the kinetic instabilities, those induced by the temperature anisotropy of the electron populations (Lazar et al., 2022; Shaaban et al., 2021; Viñas et al., 2015; Štverák et al., 2008). In the absence of particle-particle

Table 3
Parameters and Related Values Adopted for the Computation of Instability Thresholds

Events	κ	η_h	A_h ($r \geqslant 0.7$)	$\beta_{h\parallel}$	$\beta_{c\parallel}$
Slow wind	3	0.038	$0.24 + 0.79A_c$	>0.1	$0.33 + 1.73\beta_{h,\parallel}$
				<0.1	$1.04\beta_{h\parallel}^{0.36}$
	8	0.062	$0.28 + 0.73A_c$	>0.1	$0.48 + 2.3\beta_{h\parallel}$
				<0.1	$2.34\beta_{h\parallel}^{0.49}$
Fast wind	3	0.032	$0.30 + 0.74A_c$	>0.1	$0.24 + 1.19\beta_{h\parallel}$
				<0.1	$0.78\beta_{h\parallel}^{0.34}$
	8	0.042	$0.34 + 0.71A_c$	>0.1	$0.26 + 1.73\beta_{h\parallel}$
				<0.1	$0.83\beta_{h\parallel}^{0.33}$
All data	3	0.036	$0.28 + 0.77A_c$	>0.1	$0.36 + 1.46\beta_{h\parallel}$
				<0.1	$0.95\beta_{h\parallel}^{0.35}$
	8	0.055	$0.35 + 0.67A_c$	>0.1	$0.42 + 2.34\beta_{h\parallel}$
				<0.1	$2.04\beta_{h\parallel}^{0.51}$

Note. Note also that $\beta_{p\parallel} = \beta_{p\perp} = \beta_{c\parallel}/3$.

collisions, it is expected that these instabilities explain the in situ observations, which show a limitation of the anisotropies. In the case of a dominant bi-Maxwellian electron core, the theories developed early for these instabilities could be directly applied, and their threshold conditions seem to explain surprisingly well the observational bounds of temperature anisotropy (Štverák et al., 2008). Similar attempts to explain the anisotropy limits of the electron halo, markedly less dense and described by bi-Kappa distributions, have not had the same success (Shaaban et al., 2021). Here we approach these instabilities in a more in-depth manner, taking into account the influence of the core population, estimated for the first time through the core-halo correlations established in Section 2. The objective is to calculate in this way the new threshold conditions of the instabilities and to check if they become more consistent with the observations. In the present analysis, we limit ourselves to the wave instabilities parallel to the magnetic field, but we consider both the firehose instability induced by $A < 1$ and the whistler instability induced by $A > 1$. The parameterization used in the derivations below, including the correlations between the anisotropies and between the beta parameters, but also the values of the relative density η_h, can be found in Table 3.

Recall that our electron-proton plasma has two populations of electrons, the bi-Maxwellian core and the bi-Kappa halo. Štverák et al. (2008) directly determined the temperatures of the electron populations (as fitting parameters), while Lazar, Pierrard, et al. (2017) showed that these temperatures decrease with the parameter κ, according to the relationships (5) in Shaaban et al. (2019c) (See also the arguments in Lazar et al. (2015) and Lazar and Fichtner (2021)), which we also adopt here. The compact dispersion relations for parallel EM waves read (Shaaban et al., 2019c)

$$\begin{aligned}\tilde{k}^2 = \eta_h\mu\left[A_h - 1 + \frac{A_h(\tilde{\omega} \pm \mu)\mp\mu}{\tilde{k}\sqrt{\mu\chi_h\beta_{h\parallel}/\eta_h}}Z_\kappa\left(\frac{\tilde{\omega} \pm \mu}{\tilde{k}\sqrt{\mu\chi_h\beta_{h\parallel}/\eta_h}}\right)\right] + \frac{\tilde{\omega}}{\tilde{k}\sqrt{\beta_{p\parallel}}}Z_M\left(\frac{\tilde{\omega}\mp 1}{\tilde{k}\sqrt{\beta_{p\parallel}}}\right)\\ +\eta_c\mu\left[A_c - 1 + \frac{A_c(\tilde{\omega} \pm \mu)\mp\mu}{\tilde{k}\sqrt{\mu\beta_{c\parallel}/\eta_c}}Z_M\left(\frac{\tilde{\omega} \pm \mu}{\tilde{k}\sqrt{\mu\beta_{c\parallel}/\eta_c}}\right)\right],\end{aligned} \tag{2}$$

where $\tilde{k} = ck/\omega_{pp}$ is the normalized wave number k, c is the speed of light, $\chi_h = (\kappa - 1.5)/\kappa$, $\omega_{pp} = \left(4\pi n_p e^2/m_p\right)^{1/2}$ is the proton (subscript p) plasma frequency, proportional to the proton number density $n_p = n_e$ (subscript e for electrons), $\tilde{\omega} = \omega/\Omega_p$ is the normalized wave frequency ω, $\mu = m_p/m_e$ is the proton-electron mass ratio, $\Omega_j = eB_0/m_jc$ is the non-relativistic gyro-frequency of the plasma species j (with elementary charge e). Operations "±" correspond to circular right-hand (RH) or left-hand (LH) polarized waves, respectively, and the electron firehose (EFH) instability is a LH mode. Also,

$$Z_\kappa\left(\xi_j^\pm\right) = \frac{1}{\pi^{1/2}\kappa^{1/2}}\frac{\Gamma(\kappa)}{\Gamma(\kappa - 1/2)}\int_{-\infty}^{\infty}\frac{\left(1 + x^2/\kappa\right)^{-\kappa}}{x - \xi_j^\pm}dx, \Im\left(\xi_j^\pm\right) > 0, \tag{3}$$

is the modified dispersion function for a Kappa-distributed plasma (Lazar et al., 2008) of argument $\xi_j^\pm = (\omega \pm \Omega_j)/(k\theta_{j\parallel})$. In the Maxwellian limit $Z_{\kappa\to\infty}\left(\xi_j^\pm\right) = Z_M\left(\xi_j^\pm\right)$ we recover the standard plasma dispersion function (Fried & Conte, 1961)

$$Z_M\left(\xi_j^\pm\right) = \frac{1}{\sqrt{\pi}}\int_{-\infty}^{\infty}\frac{\exp\left(-x^2\right)}{x - \xi_j^\pm}dx, \Im\left(\xi_j^\pm\right) > 0. \tag{4}$$

For whistler modes the wave frequencies are much higher than the proton gyro-frequency $\Omega_p \ll \omega_r < |\Omega_e|$ (protons do not interact with whistlers), and their dispersion relation can be reduced to

Table 4
Fitting Parameters for Core Thresholds

		Whistler		Firehose	
Events	κ	α	s	α	s
Slow wind	3	0.171	0.662	−1.413	1.029
	8	0.192	0.609	−1.545	1.045
Fast wind	3	0.123	0.959	−1.215	0.969
	8	0.104	1.178	−1.338	0.957
Total data	3	0.152	0.726	−1.377	1.004
	8	0.183	0.695	−1.534	1.013
BM	∞	0.251	0.512	−1.750	1.041

$$\tilde{k}^2 = \eta_h\left[A_h - 1 + \frac{A_h(\tilde{\omega}-1)+1}{\tilde{k}\sqrt{\chi_h\beta_{h\|}/\eta_h}}Z_\kappa\left(\xi_h^-\right)\right] + \eta_c\left[A_c - 1 + \frac{A_c(\tilde{\omega}-1)+1}{\tilde{k}\sqrt{\beta_{c\|}/\eta_c}}Z_M\left(\xi_c^-\right)\right] \tag{5}$$

this time with $\xi_h^- = (\tilde{\omega}-1)/\left(\tilde{k}\sqrt{\chi_h\beta_{h\|}/\eta_h}\right)$, $\xi_c^- = (\tilde{\omega}-1)/\left(\tilde{k}\sqrt{\beta_{c\|}/\eta_c}\right)$, $\tilde{k} = ck/\omega_{pe}$, the electron plasma frequency $\omega_{pe} = \left(4\pi n_e e^2/m_e\right)^{1/2}$, and the normalized wave frequency $\tilde{\omega} = \omega/|\Omega_e|$.

Instability thresholds are isocontours of low levels of maximum growth rates ($\gamma_m \rightarrow 0$, near marginal stability) in the parametric space A versus $\beta_\|$. Here, the thresholds for the EFH instability are derived for $\gamma = 10^{-3}\Omega_p$, and those of the whistler instability (WI) for $\gamma = 10^{-3}|\Omega_e|$. They are fitted to an inverse power law of the form

$$A_j = 1 + \frac{\alpha}{\beta_j^s} \tag{6}$$

The fitting parameters, α and s, are distinctively derived, first in terms of the core ($j = c$) parameters (A_c vs. $\beta_{c\|}$), and then in terms of the halo ($j = h$) parameters (A_h vs. $\beta_{h\|}$), and their values are tabulated in Tables 4 and 5, respectively. We choose to derive these thresholds for two different values of the parameter κ, namely $\kappa = 3$ (red contours) and $\kappa = 8$ (green contours), using the corresponding correlations found in the previous section for the anisotropies and for the beta parameters, and also the relative densities η_h. Table 3 shows these values for each individual case, while the corresponding fitting parameters, α and s, can be found in Tables 4 and 5.

The new threshold contours are plotted in Figure 5, compared with the density plots of electron events, the halo (left) and the core (right), counted by the adjacent logarithmic color bars. Notice again that for firehose instability the thresholds are those calculated for $A < 1$, while for whistler instability the thresholds are those obtained for $A > 1$. We are particularly interested in the events in the slow solar wind (top panels) because they are less affected by the strahl, the third electron component that is not captured in the present analysis. However, we also continue to compare the thresholds obtained for the fast solar wind (middle panels) and for all data (bottom panels) with the corresponding events. To highlight mutual effects, the threshold contours obtained for independent or not correlated (NC) (For the NC case, we adopt the following plasma parameters: $\eta_h = 0.035, \beta_{c\|} = 0.5, A_c = 1.2$ for whistler instability, and $\eta_h = 0.035, \beta_{c\|} = 2.0, A_c = 0.8$ for firehose instability) bi-Kappa and bi-Maxwellian populations, that is, in the absence of mutual effects (Lazar, Shaaban, et al., 2017; Lazar et al., 2015; Štverák et al., 2008), are also displayed. For $\kappa = 8$ the threshold obtained for the halo electrons is practically the same as (or indistinguishable from) the one obtained in the bi-Maxwellian limit. Thus, we can appreciate that the anisotropy thresholds are generally reduced under the mutual effects of the electron populations. Those specific to the halo (left panels) even drop considerably under the effect of the core populations, an otherwise expected effect, considering the dominance of the high-dense core.

Table 5
Fitting Parameters for Halo Thresholds

		Whistler		Firehose	
Events	κ	α	s	α	s
Slow wind	3	0.108	0.349	−0.489	0.970
	8	0.087	0.295	−0.367	0.888
Fast wind	3	0.120	0.345	−0.638	1.050
	8	0.089	0.455	−0.446	1.059
Total data	3	0.109	0.375	−0.521	0.996
	8	0.078	0.381	−0.341	0.939
NC	3	0.104	0.450	−1.778	1.378

In the slow solar wind, the new thresholds model very well the edges of the halo anisotropy from the quasi-stable events reported by the observations. The results have maximum relevance in this case, considering the minimal role of particle-particle collisions for halo electrons with high energy and low density. Instead, we see that self-generated instabilities are those that can constrain and self-organize the temperature anisotropy. Although these thresholds do not vary much with the parameter κ, it can still be observed that the effect of the core is more pronounced when κ is higher (green contour for $\kappa = 8$), that is, when the halo is more thermalized. An apparently natural effect, considering that in this case the halo is more similar to the core. Instead, a more energetic halo with $\kappa = 3$ acts more strongly on the core, in which case the threshold (red

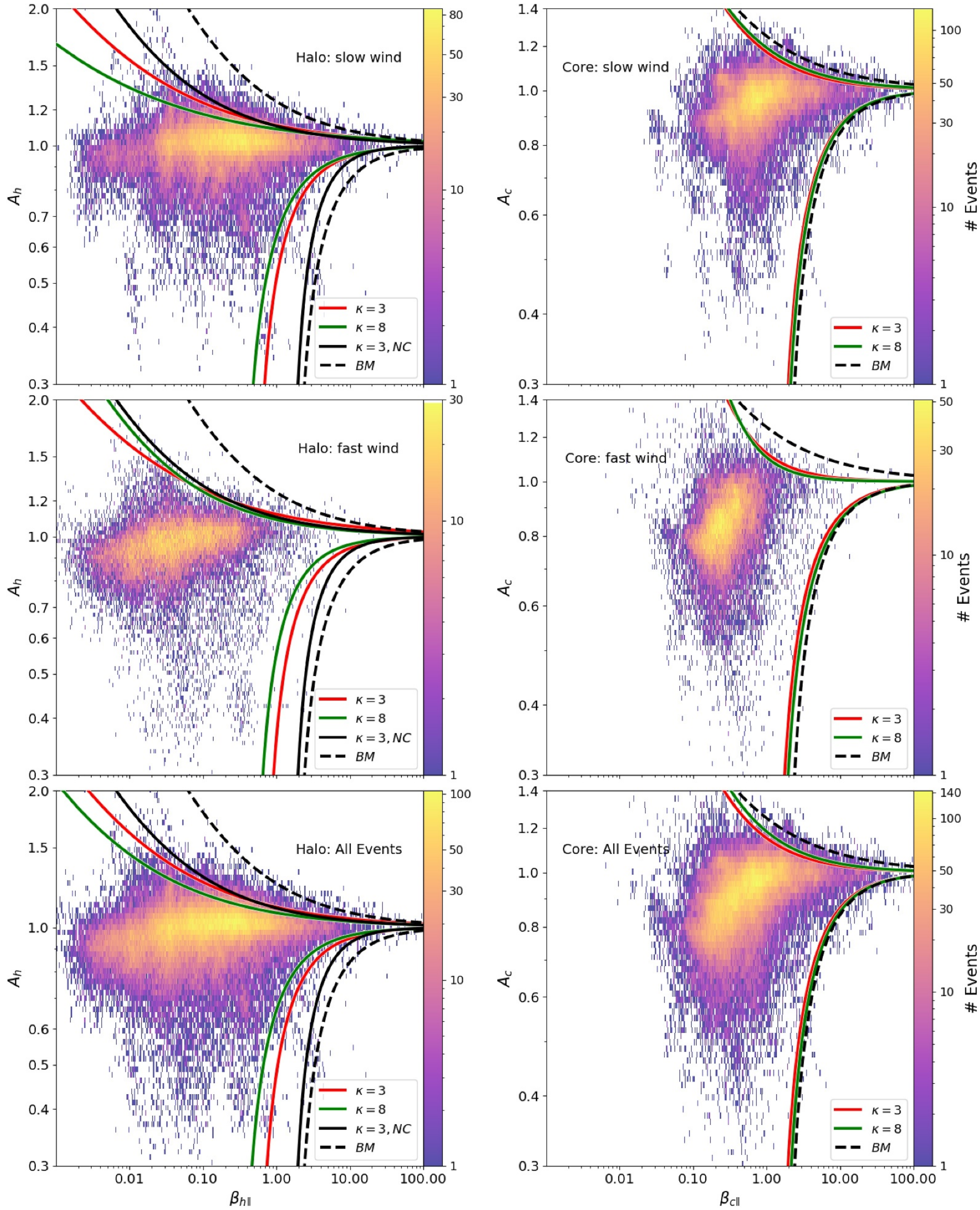

Figure 5. Thresholds $(\gamma = 10^{-3}|\Omega_{p,e}|)$ of whistler ($A > 1$) and firehose ($A < 1$) instabilities in the slow wind (upper), fast wind (middle) and all events (lower) for the electron halo in terms of A_h versus $\beta_{h,\|}$ (left), and for the electron core in terms of A_c versus $\beta_{c,\|}$ (right). Parameters used to derive the instability thresholds are summarized in Table 3.

contour) is lower than for $\kappa = 8$ (green contour). A similar discussion supports the bottom panels, where all data from the solar wind are considered. In this case as well, the new thresholds thus obtained can explain the limits of the temperature anisotropy from the in situ observations. This is explained by the fact that the data from the fast solar wind (middle panels) are narrower, generally at lower anisotropies. From the fairly good comparison of the whistler instability thresholds with the data, it can still be seen that it represents a plausible mechanism to constrain both anisotropies $A_{c,h} > 1$. However, the new thresholds remain less connected to the observational data from the fast solar wind, in the case of firehose instability still far from the limits of anisotropy $A_{c,h} < 1$. The origin of these differences is probably the electron strahl aligned with the magnetic field, also an important source of free kinetic energy, especially for the firehose instability (Shaaban et al., 2018), but whose properties were not provided by Štverák et al. (2008) to be included in the present analysis.

4. Conclusions

In space plasmas, although electrons undergo rare collisions, in situ observations reveal relatively small temperature anisotropies. In this case, major deviations from isotropy are expected to be constrained by self-generated kinetic instabilities, which classical theories seem to confirm, but only for the bi-Maxwellian electrons in the low-energy core (Štverák et al., 2008). The other major component in the observed electron VDs is the suprathermal halo described by the bi-Kappa distributions, which is less dense but much hotter and may extend to larger temperature anisotropies. The existing attempts to explain their bounds are not satisfactory, but suggest refining the analysis by including the mutual core-halo effects.

In this paper, we have provided such a new kinetic approach, based on observational estimates of the correlations between the two populations. These correlations were derived for the main parameters used in the analysis of instabilities, such as temperature anisotropies and beta parameters. We have exploited the large data set produced by Štverák et al. (2008), which characterizes the electron core and halo populations from about 1.2×10^5 events at low (ecliptic) latitudes but a wide range of heliocentric distances, from 0.3 to about 4.0 AU. The electron events exhibit a high degree of linear correlation of the core and halo anisotropies, $A_h = mA_c + q$; values obtained for the parameters m and q were given in Figure 2, and also Figures A1–A3 from Appendix A. Although these correlations may vary with the slow or fast nature of the solar wind, also with the parameter κ and implicitly the heliocentric distance, the vast majority of events, that is, more than 75% remain highly correlated ($r \geqslant 0.7$), while more than 40% are very highly correlated ($r \geqslant 0.9$). Such direct correlations between A_h and A_c can be motivated by physical mechanisms that generally act the same on the two populations. We can thus recall the magnetic compression or the interaction with cyclotron EM waves, which can both lead to $A_{h,c} > 1$, but also the expansion of the solar wind plasma or the interaction with hybrid waves (with a major component of the electric field parallel to the magnetic field), which can both lead to $A_{h,c} < 1$.

The beta parameters of the core $(\beta_{c\|})$ and the halo $(\beta_{h\|})$ appear to be even better correlated, but with a bimodal profile, depending on the values of these parameters. First of all, the events in the ecliptic are found to be dominated by the core population with $\beta_{c\|} \geqslant \beta_{h\|}$, always lying above the first diagonal $\beta_{c\|} = \beta_{h\|}$ (kinetic energy equipartition). Following the bimodal profile of the event distribution, we first determined a power-law fitting regression, $\beta_{c\|} = a\beta_{h\|}^b$, for the small values arm of $\beta_{c\|} < 0.1$ and $\beta_{h\|} < 0.1$. The events of the other arm of large $\beta_{c\|} > 0.1$ and $\beta_{h\|} > 0.1$, tend to align (but remain above) the condition $\beta_{c\|} = \beta_{h\|}$, and have been fitted to a linear regression $\beta_{c\|} = c + d\beta_{h\|}$. The values of these fitting parameters (a, b, c and d) are given in each panel of Figure 3, and their variations with the nature of the slow or fast solar wind and with the kappa parameter are not significant. In this case, we did not invoke Pearson coefficients for a correlation statistic because the events are less scattered, aligning much better along the regression fits.

Finally, we used the core-halo correlations to numerically determine the threshold conditions for two representative instabilities, the whistler instability (specific for $A > 1$) and the firehose instability (triggered by $A < 1$). These correlations made it possible to obtain the instability thresholds as functions only of the core parameters (A_c vs. $\beta_{c\|}$), or as functions only of the halo parameters (A_h vs. $\beta_{h\|}$). In each of these two situations, the anisotropy thresholds incorporate mutual core-halo effects. Only these thresholds justify the comparison in Figure 5 with the observational data, A_c versus $\beta_{c\|}$ that describe the core electrons, or with the halo data A_h versus $\beta_{h\|}$. To characterize these instabilities, we also used the average values of the relative density of the halo population $\eta_h = n_h/n_e (=1 - n_c/n_e)$, which also exhibits a bimodal dependence of κ, with lower (average) values for $\kappa < 6$, and higher (average) values for $\kappa > 6$.

Compared with observations (Figure 5), the new thresholds obtained here are found to shape the limits of the halo anisotropy very well, and also the margins of the core anisotropy. These results are particularly relevant for slow solar wind events (upper panels) because the strahl (not treated here) does not have much influence, and also for all data (bottom panels), including the fast wind events, which are, however, less widespread. These results are the most consistent and suggestive obtained so far regarding the constraining role played by these instabilities on the electron temperature anisotropy. Whistler instabilities can still play such a role in constraining anisotropy $A > 1$ even in the fast solar wind, as suggested by the middle panels in Figure 5. These data are somewhat more restrained at lower beta parameters, most likely because of the subcoronal origin of the high-speed winds.

Moreover, the third component, namely the field-aligned strahl, is commonly more prominent in the fast solar wind, contributing to the self-induced small-scale turbulence via kinetic instabilities. Cumulating the effect of the strahl with that of firehose instability induced by $A < 1$, could determine (much) lower threshold conditions than those derived here, and probably good enough to explain the limits of this temperature anisotropy in the fast solar wind (middle panels in Figure 5). For further definitive answers in such cases, it is still necessary to quantify the properties of the main electron populations (core, halo, and strahl) in the high-speed winds. The present results should also stimulate future extended analyzes at higher latitudes outside the ecliptic, explored in the past by the Ulysses mission and currently completed by the Solar Orbiter, but also in the young solar wind, inside 0.3 AU, with the data transmitted by Parker Solar Probe. Nevertheless, correlations between electron populations can still be invoked to upgrade more extensive quasi-linear analyses, which can produce dynamical trajectories of relaxation of the initial anisotropies for both the core and the electron halo (Sarfraz, 2018; Sarfraz et al., 2016; Shaaban et al., 2019b, 2019c).

Appendix A: Temperature Anisotropies as a Function of κ

Similarly to Figure 2, here in Figures A1–A3 we show additional detailed plots aiming to differentiate between A_h and A_c, but also between their correlations, as a function of the parameter κ. The variation of κ from small to large values can be associated with a decrease in the heliocentric distance, small values such as $\kappa = 3$ being specific for

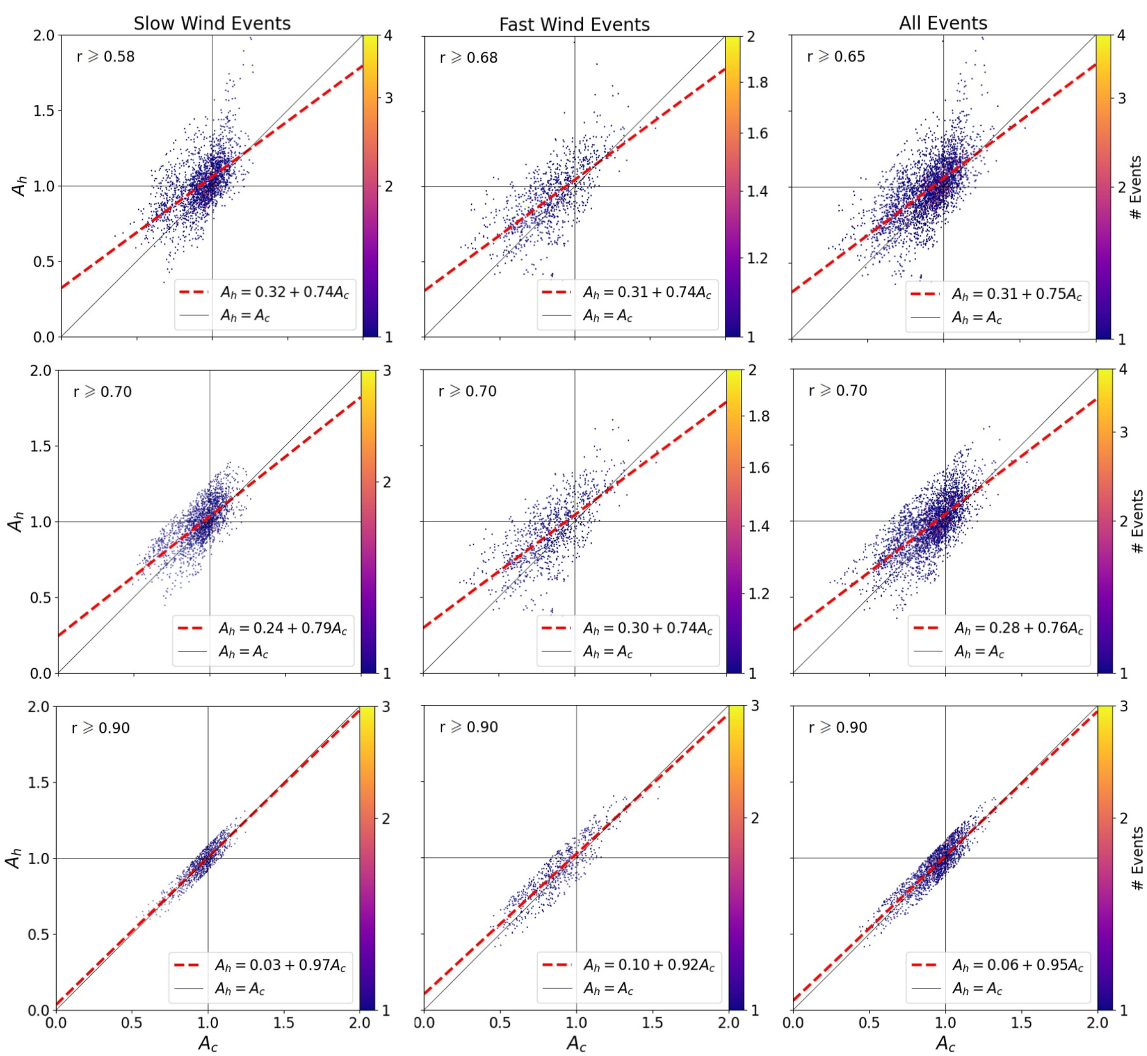

Figure A1. As in Figure 2 but only the events with $\kappa \in [2.7, 3.3]$, more specific to large heliocentric distances, that is, >1 AU (Lazar et al., 2020; Pierrard et al., 2016).

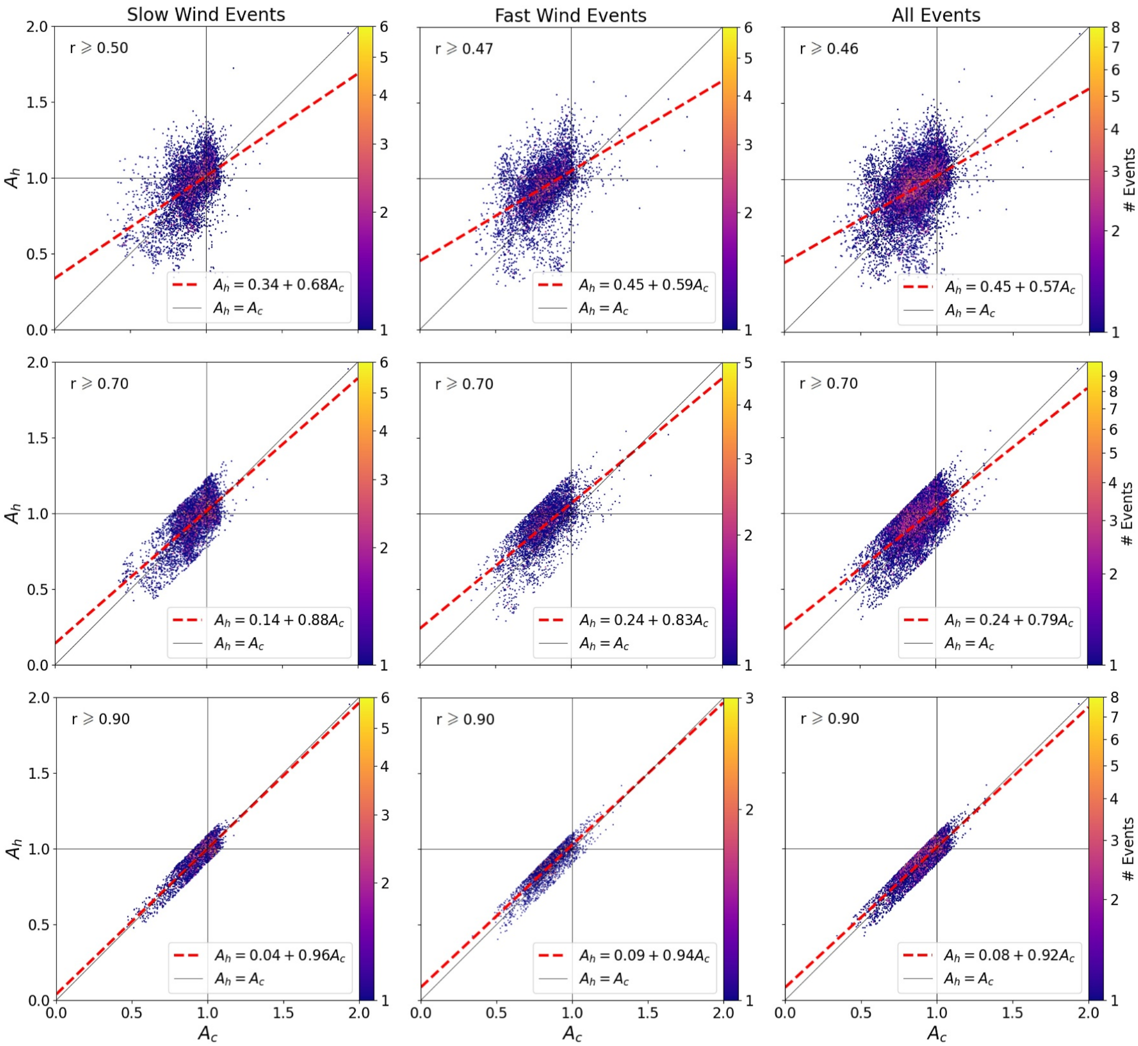

Figure A2. As in Figure 2 but only the events with $\kappa \in [4.5, 5.5]$, more specific to moderate heliocentric distances, that is, ∼1 AU (Lazar et al., 2020; Pierrard et al., 2016).

large distances beyond 1.0 AU, while large $\kappa > 6$ are predominantly found at distances, below 1.0 AU (Lazar et al., 2020; Pierrard et al., 2016). The linear regression fit, $A_h = mA_c + q$ (red dashed line), does not show large deviations from the ideal linear correlation, $A_h = A_c$ (first diagonal, with black solid line), and the values found for the fit parameters m and q are given in the legend of each panel. Although the differences are not major and the number of events decreases significantly with decreasing κ, there is still a trend that should be mentioned, because it is somewhat unexpected: the anisotropies become less correlated when the halo is more thermalized, that is, at higher values of κ.

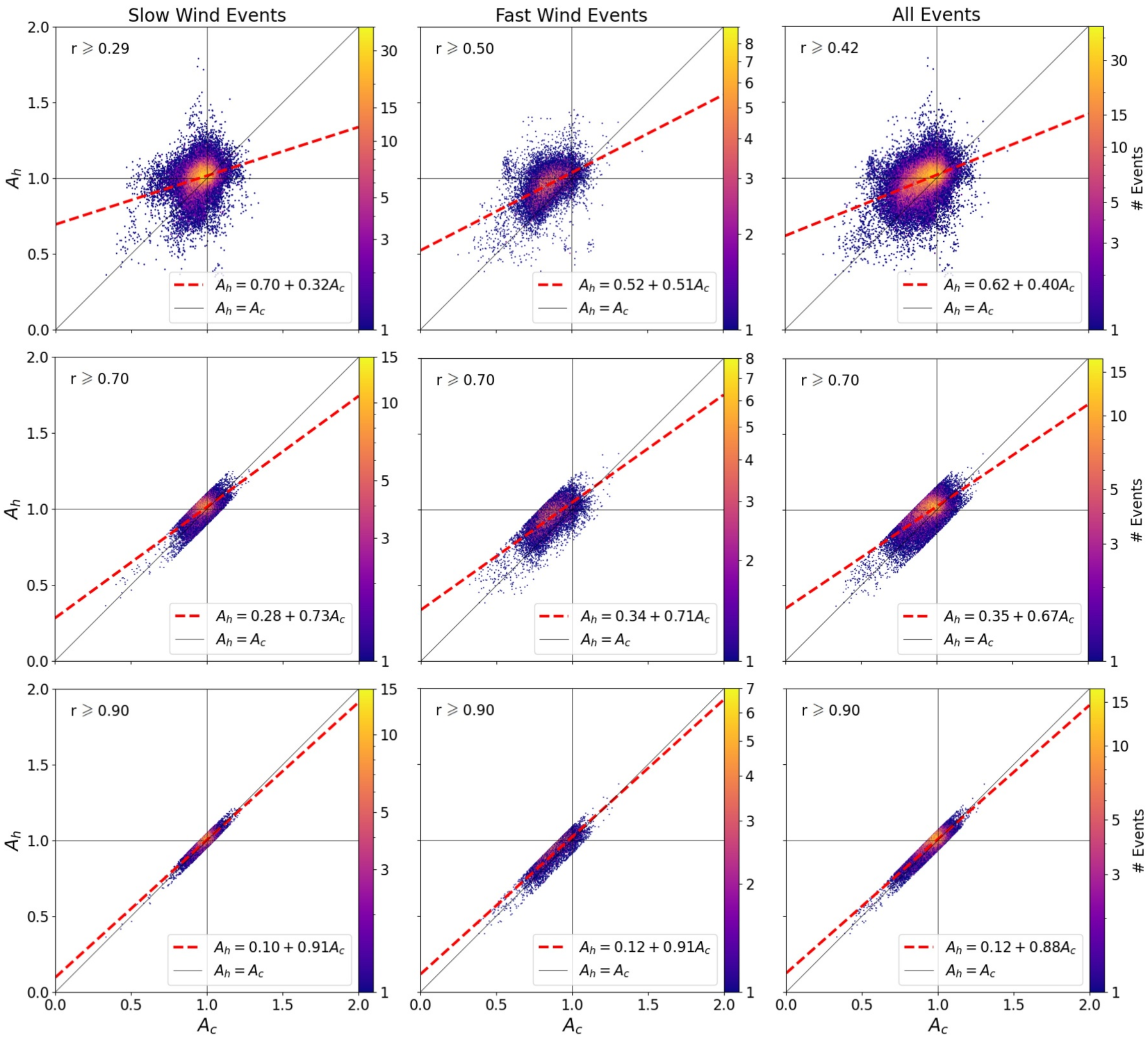

Figure A3. As in Figure 2 but only the events with $\kappa \geqslant 6$, specific to low heliocentric distances, that is, <0.7 AU (Lazar et al., 2020; Pierrard et al., 2016).

Acknowledgments
The authors acknowledge support from Katholieke Universiteit Leuven, Ruhr-University Bochum, and Qatar University. These results were obtained in the framework of the projects C16/24/010 (C1 project Internal Funds KU Leuven), WEAVE project G002523N (FWO-Vlaanderen), 4000145223 SIDC Data Exploitation (SIDEX2), ESA Prodex, Belspo project B2/191/P1/SWiM. Powered@NLHPC: This research was partially supported by the supercomputing infrastructure of the NLHPC (CCSS210001). The resources and services used in this work were provided by the VSC (Flemish Supercomputer Center), funded by the Research Foundation—Flanders (FWO) and the Flemish Government. The project 21GRD02 BIOSPHERE has received funding from the European Partnership on Metrology, co-financed by the European Union's Horizon Europe Research and

Data Availability Statement

The electron data used in this paper were provided by the authors of Štverák et al. (2008), while the raw electron data can also be accessed through the SPFD CDA Web service cdaweb.gsfc.nasa.gov. The entire Helios data set is archived and maintained at the University of California Berkeley: https://helios-data.ssl.berkeley.edu. Plots were produced with Matplotlib, available under the Matplotlib license at https://matplotlib.org/. The relevant Python scripts are available at Shaaban et al. (2025).

References

Abraham, J. B., Owen, C. J., Verscharen, D., Bakrania, M., Stansby, D., Wicks, R. T., et al. (2022). Radial evolution of thermal and suprathermal electron populations in the slow solar wind from 0.13 to 0.5 au: Parker solar probe observations. *The Astrophysical Journal*, *931*(2), 118. https://doi.org/10.3847/1538-4357/ac6605

Bale, S. D., Kasper, J. C., Howes, G. G., Quataert, E. C. S., & Sundkvist, D. (2009). Magnetic fluctuation power near proton temperature anisotropy instability thresholds in the solar wind. *Physical Review Letters*, *103*(21), 211101. https://doi.org/10.1103/PhysRevLett.103.211101

Berčič, L., Maksimović, M., Landi, S., & Matteini, L. (2019). Scattering of strahl electrons in the solar wind between 0.3 and 1 au: Helios observations. *Monthly Notices of the Royal Astronomical Society*, *486*(3), 3404–3414. https://doi.org/10.1093/mnras/stz1007

Fried, B., & Conte, S. (1961). *The plasma dispersion function*. Academic Press. https://doi.org/10.1016/B978-1-4832-2929-4.50005-8

Gary, S. P. (1993). *Theory of space plasma microinstabilities*. Cambridge University Press. https://doi.org/10.1017/CBO9780511551512

Hinkle, D., Wiersma, W., & Jurs, S. (2003). *Applied statistics for the behavioral sciences (No. v. 663)*. Houghton Mifflin. Retrieved from https://books.google.de/books?id=7tntAAAAMAAJ

Innovation Programme and by the Participating States. The open access publication of this article was funded by Qatar National Library.

Huang, J., Kasper, J. C., Vech, D., Klein, K. G., Stevens, M., Martinović, M. M., et al. (2020). Proton temperature anisotropy variations in inner heliosphere estimated with the first parker solar probe observations. *The Astrophysical Journal - Supplement Series*, *246*(2), 70. https://doi.org/10.3847/1538-4365/ab74e0

Lazar, M., & Fichtner, H. (2021). Kappa distribution function: From empirical to physical concepts. In M. Lazar & H. Fichtner (Eds.), *Kappa distributions: From observational evidences via controversial predictions to a consistent theory of nonequilibrium plasmas* (pp. 107–123). Springer International Publishing. https://doi.org/10.1007/978-3-030-82623-9_6

Lazar, M., López, R. A., Shaaban, S. M., Poedts, S., Yoon, P. H., & Fichtner, H. (2022). Temperature anisotropy instabilities stimulated by the solar wind suprathermal populations. *Frontiers in Astronomy and Space Sciences*, *8*, 249. https://doi.org/10.3389/fspas.2021.777559

Lazar, M., Pierrard, V., Poedts, S., & Fichtner, H. (2020). Characteristics of solar wind suprathermal halo electrons. *Astronomy & Astrophysics*, *642*, A130. https://doi.org/10.1051/0004-6361/202038830

Lazar, M., Pierrard, V., Shaaban, S. M., Fichtner, H., & Poedts, S. (2017). Dual Maxwellian-Kappa modeling of the solar wind electrons: New clues on the temperature of Kappa populations. *Astronomy & Astrophysics*, *602*, A44. https://doi.org/10.1051/0004-6361/201630194

Lazar, M., Poedts, S., & Fichtner, H. (2015). Destabilizing effects of the suprathermal populations in the solar wind. *Astronomy & Astrophysics*, *582*, A124. https://doi.org/10.1051/0004-6361/201526509

Lazar, M., Schlickeiser, R., & Shukla, P. K. (2008). Cumulative effect of the weibel-type instabilities in symmetric counterstreaming plasmas with kappa anisotropies. *Physics of Plasmas*, *15*(4), 042103. https://doi.org/10.1063/1.2896232

Lazar, M., Shaaban, S. M., Fichtner, H., & Poedts, S. (2018). Temperature anisotropy instabilities stimulated by the interplay of the core and halo electrons in space plasmas. *Physics of Plasmas*, *25*(2), 022902. https://doi.org/10.1063/1.5016261

Lazar, M., Shaaban, S. M., Poedts, S., & Štverák, Š. (2017). Firehose constraints of the bi-Kappa-distributed electrons: A zero-order approach for the suprathermal electrons in the solar wind. *Monthly Notices of the Royal Astronomical Society*, *464*(1), 564–571. https://doi.org/10.1093/mnras/stw2336

Maksimovic, M., Walsh, A. P., Pierrard, V., Štverák, Š., & Zouganelis, I. (2021). Electron Kappa distributions in the solar wind: Cause of the acceleration or consequence of the expansion? In M. Lazar & H. Fichtner (Eds.), *Kappa distributions; from observational evidences via controversial predictions to a consistent theory of nonequilibrium plasmas* (Vol. 464, pp. 39–51). https://doi.org/10.1007/978-3-030-82623-9_3

Maksimovic, M., Zouganelis, I., Chaufray, J. Y., Issautier, K., Scime, E. E., Littleton, J. E., et al. (2005). Radial evolution of the electron distribution functions in the fast solar wind between 0.3 and 1.5 AU. *Journal of Geophysical Research*, *110*(A9), A09104. https://doi.org/10.1029/2005JA011119

Matteini, L., Landi, S., Hellinger, P., Pantellini, F., Maksimovic, M., Velli, M., et al. (2007). Evolution of the solar wind proton temperature anisotropy from 0.3 to 2.5 AU. *Geophysical Research Letters*, *34*(20), L20105. https://doi.org/10.1029/2007GL030920

Micera, A., Boella, E., Zhukov, A. N., Shaaban, S. M., López, R. A., Lazar, M., & Lapenta, G. (2020). Particle-in-cell simulations of the parallel proton firehose instability influenced by the electron temperature anisotropy in solar wind conditions. *The Astrophysical Journal*, *893*(2), 130. https://doi.org/10.3847/1538-4357/ab7faa

Pierrard, V., & Lazar, M. (2010). Kappa distributions: Theory and applications in space plasmas. *Solar Physics*, *267*(1), 153–174. https://doi.org/10.1007/s11207-010-9640-2

Pierrard, V., Lazar, M., & Štverák, S. (2020). Solar wind plasma particles organized by the flow speed. *Solar Physics*, *295*(11), 151. https://doi.org/10.1007/s11207-020-01730-z

Pierrard, V., Lazar, M., & Stverak, S. (2022). Implications of Kappa suprathermal halo of the solar wind electrons. *Frontiers in Astronomy and Space Sciences*, *9*, 892236. https://doi.org/10.3389/fspas.2022.892236

Pierrard, V., Lazar, M., Poedts, S., Štverák, Š., Maksimovic, M., & Trávníček, P. M. (2016). The electron temperature and anisotropy in the solar wind. Comparison of the core and halo populations. *Solar Physics*, *291*(7), 2165–2179. https://doi.org/10.1007/s11207-016-0961-7

Pierrard, V., Lemaire, J., Heynderickx, D., Kruglanski, M., Looper, M., Blake, B., & Mewaldt, D. (2000). Statistical analysis of SAMPEX PET proton measurements. *Nuclear Instruments and Methods in Physics Research*, *449*(1–2), 378–382. https://doi.org/10.1016/S0168-9002(99)01454-0

Sarfraz, M. (2018). A moment-based quasilinear theory for electron firehose instability driven by solar wind core/halo electrons. *Journal of Geophysical Research: Space Physics*, *123*(8), 6107–6118. https://doi.org/10.1029/2018JA025449

Sarfraz, M., Saeed, S., Yoon, P. H., Abbas, G., & Shah, H. A. (2016). Macroscopic quasi-linear theory of electromagnetic electron cyclotron instability associated with core and halo solar wind electrons. *Journal of Geophysical Research: Space Physics*, *121*(10), 9356–9368. https://doi.org/10.1002/2016JA022854

Shaaban, S. M., Kennis, S., Lazar, M., Pierrard, V., & Poedts, S. (2025). Core-halo correlations of solar wind electrons and temperature anisotropy instabilities [Software]. *Zenodo*. https://doi.org/10.5281/zenodo.14839786

Shaaban, S. M., Lazar, M., López, R. A., Fichtner, H., & Poedts, S. (2019a). Firehose instabilities triggered by the solar wind suprathermal electrons. *Monthly Notices of the Royal Astronomical Society*, *483*(4), 5642–5648. https://doi.org/10.1093/mnras/sty3377

Shaaban, S. M., Lazar, M., López, R. A., Yoon, P. H., & Poedts, S. (2021). Advanced interpretation of waves and instabilities in space plasmas. In M. Lazar & H. Fichtner (Eds.), *Kappa distributions: From observational evidences via controversial predictions to a consistent theory of nonequilibrium plasmas* (pp. 185–218). Springer International Publishing. https://doi.org/10.1007/978-3-030-82623-9_10

Shaaban, S. M., Lazar, M., Yoon, P. H., & Poedts, S. (2018). Beaming electromagnetic (or heat-flux) instabilities from the interplay with the electron temperature anisotropies. *Physics of Plasmas*, *25*(8), 082105. https://doi.org/10.1063/1.5042481

Shaaban, S. M., Lazar, M., Yoon, P. H., & Poedts, S. (2019b). Quasilinear approach of the cumulative whistler instability in fast solar wind: Constraints of electron temperature anisotropy. *Astronomy & Astrophysics*, *627*, A76. https://doi.org/10.1051/0004-6361/201935515

Shaaban, S. M., Lazar, M., Yoon, P. H., & Poedts, S. (2019c). The interplay of the solar wind core and suprathermal electrons: A quasilinear approach for firehose instability. *The Astrophysical Journal*, *871*(2), 237. https://doi.org/10.3847/1538-4357/aaf72d

Štverák, Š., Maksimovic, M., Trávníček, P. M., Marsch, E., Fazakerley, A. N., & Scime, E. E. (2009). Radial evolution of nonthermal electron populations in the low-latitude solar wind: Helios, cluster, and Ulysses observations. *Journal of Geophysical Research*, *114*(A5), A05104. https://doi.org/10.1029/2008JA013883

Štverák, Š., Trávníček, P., Maksimovic, M., Marsch, E., Fazakerley, A. N., & Scime, E. E. (2008). Electron temperature anisotropy constraints in the solar wind. *Journal of Geophysical Research*, *113*(A3). https://doi.org/10.1029/2007JA012733

Verscharen, D., Chandran, B. D. G., Boella, E., Halekas, J., Innocenti, M. E., Jagarlamudi, V. K., et al. (2022). Electron-driven instabilities in the solar wind. *Frontiers in Astronomy and Space Sciences*, *9*, 951628. https://doi.org/10.3389/fspas.2022.951628

Verscharen, D., Chandran, B. D. G., Jeong, S.-Y., Salem, C. S., Pulupa, M. P., & Bale, S. D. (2019). Self-induced scattering of strahl electrons in the solar wind. *The Astrophysical Journal*, *886*(2), 136. https://doi.org/10.3847/1538-4357/ab4c30

Verscharen, D., Klein, K. G., & Maruca, B. A. (2019). The multi-scale nature of the solar wind. *Living Reviews in Solar Physics*, *16*(1), 5. https://doi.org/10.1007/s41116-019-0021-0

Viñas, A. F., Moya, P. S., Navarro, R. E., Valdivia, J. A., Araneda, J. A., & Muñoz, V. (2015). Electromagnetic fluctuations of the whistler-cyclotron and firehose instabilities in a Maxwellian and Tsallis-Kappa-like plasma. *Journal of Geophysical Research: Space Physics*, *120*(5), 3307–3317. https://doi.org/10.1002/2014JA020554

Vocks, C., Mann, G., & Rausche, G. (2008). Formation of suprathermal electron distributions in the quiet solar corona. *Astronomy & Astrophysics*, *480*(2), 527–536. https://doi.org/10.1051/0004-6361:20078826

Wilson, L. B., Chen, L.-J., Wang, S., Schwartz, S. J., Turner, D. L., Stevens, M. L., et al. (2019a). Electron energy partition across interplanetary shocks. II. Statistics. *The Astrophysical Journal - Supplement Series*, *245*(2), 24. https://doi.org/10.3847/1538-4365/ab5445

Wilson, L. B., Chen, L.-J., Wang, S., Schwartz, S. J., Turner, D. L., Stevens, M. L., et al. (2019b). Electron energy partition across interplanetary shocks. I. Methodology and data product. *The Astrophysical Journal - Supplement Series*, *243*(1), 8. https://doi.org/10.3847/1538-4365/ab22bd

Yoon, P. H., Kim, S., Choe, G. S., & moon, Y. J. (2016). Revised model of the steady-state solar wind halo electron velocity distribution function. *The Astrophysical Journal*, *826*(2), 204. https://doi.org/10.3847/0004-637X/826/2/204